Article

Femtosecond laser writing of lithium niobate ferroelectric nanodomains

https://doi.org/10.1038/s41586-022-05042-z

Received: 20 January 2022

Accepted: 29 June 2022

Published online: 14 September 2022

Check for updates

Xiaoyi Xu[1,8], Tianxin Wang[1,8], Pengcheng Chen[1], Chao Zhou[1], Jianan Ma[1], Dunzhao Wei[1,2], Huijun Wang[1,7], Ben Niu[1], Xinyuan Fang[3,4], Di Wu[1,5], Shining Zhu[1], Min Gu[3,4], Min Xiao[1,6] & Yong Zhang[1]✉

Lithium niobate ($LiNbO_3$) is viewed as a promising material for optical communications and quantum photonic chips[1,2]. Recent breakthroughs in $LiNbO_3$ nanophotonics have considerably boosted the development of high-speed electro-optic modulators[3–5], frequency combs[6,7] and broadband spectrometers[8]. However, the traditional method of electrical poling for ferroelectric domain engineering in optic[9–13], acoustic[14–17] and electronic applications[18,19] is limited to two-dimensional space and micrometre-scale resolution. Here we demonstrate a non-reciprocal near-infrared laser-writing technique for reconfigurable three-dimensional ferroelectric domain engineering in $LiNbO_3$ with nanoscale resolution. The proposed method is based on a laser-induced electric field that can either write or erase domain structures in the crystal, depending on the laser-writing direction. This approach offers a pathway for controllable nanoscale domain engineering in $LiNbO_3$ and other transparent ferroelectric crystals, which has potential applications in high-efficiency frequency mixing[20,21], high-frequency acoustic resonators[14–17] and high-capacity non-volatile ferroelectric memory[19,22].

$LiNbO_3$ crystals feature excellent electro-optic, acoustic-optic and non-linear-optic characteristics, providing a promising material platform to fabricate high-performance integrated photonic devices for next-generation optical communication networks[3–5], microwave photonic systems[23] and quantum information processing[24–27]. The advanced requirements for $LiNbO_3$ devices have pushed the development of two important fabrication techniques. One is the standard lithography and etching technique[5,13,26–29], which aims to control the propagation of light through linear susceptibility $\chi^{(1)}$-modulated $LiNbO_3$ structures such as waveguides[5,26,27], microdisks[29] and photonic crystals[5,13,28]. Benefiting from recent breakthroughs in $LiNbO_3$-on-insulator nanofabrication, the feature size of $\chi^{(1)}$-modulated $LiNbO_3$ photonic structures is reduced down to a few hundred nanometres[1,5,26], which considerably improves the performance of $LiNbO_3$ integrated devices, including high-speed electro-optic modulators[4,5].

The other fabrication technique is $LiNbO_3$ ferroelectric domain engineering[30–32], which is capable of manipulating non-linear optical processes by spatially changing the sign of second-order susceptibility $\chi^{(2)}$ in the poled $LiNbO_3$ domain structures. This technique can be used to enhance laser frequency conversion efficiency through the quasi-phase-matching (QPM) principle[33], which has been extensively investigated in the fields of non-linear[9–11,34] and quantum optics[24,27]. In addition to optical applications, $LiNbO_3$ ferroelectric domain structures are also very useful in acoustic resonators[14–17] and filters[35], as well as in non-volatile ferroelectric domain wall memory[19,22] and field-effect transistors[18]. However, electrical-field poled $LiNbO_3$ ferroelectric domain structures have been stuck in two-dimensional (2D) patterns with a micrometre resolution for decades, which severely impedes the further developments of advanced photonic, acoustic and electronic devices based on $LiNbO_3$ ferroelectric domains. Potential nanotechnologies, such as probe-tip poling[36], electron-beam poling[37,38] and light-induced domain self-assembling[39,40], are only capable of producing domain structures at the surface of $LiNbO_3$ crystals. Femtosecond laser-writing methods[41–44] have been widely applied in the fabrications of photonics structures in transparent materials. For example, they are used to produce $LiNbO_3$ domain structures with features of a few micrometres[45–50], which are difficult to further reduce because of the diffraction limit of light. It is still a great challenge to feasibly and controllably fabricate three-dimensional (3D) nanosized ferroelectric domains in $LiNbO_3$ crystals.

In this Article, we propose and experimentally demonstrate a new non-reciprocal near-infrared (NIR) laser-writing technique to perform 3D $LiNbO_3$ nanodomain engineering in a reconfigurable way. Unlike traditional ultrafast laser-writing techniques, the proposed laser-induced domain engineering strongly depends on the laser-writing direction. The basic principle can be understood from the laser-induced electric field (Fig. 1). Under our experimental conditions, the thermoelectric field is the dominant effect used to laser write a domain structure (with a contribution from the pyroelectric effect, see Methods). At the focal point of the laser beam, multiphoton absorption of NIR light produces a localized temperature field, in which two physical mechanisms dominate the light–$LiNbO_3$-domain interaction. First, the tightly focused

[1]National Laboratory of Solid State Microstructures, College of Engineering and Applied Sciences, School of Physics, Collaborative Innovation Center of Advanced Microstructures, Nanjing University, Nanjing, China. [2]School of Physics, Sun Yat-sen University, Guangzhou, China. [3]Institute of Photonic Chips, University of Shanghai for Science and Technology, Shanghai, China. [4]Centre for Artificial-Intelligence Nanophotonics, School of Optical-Electrical and Computer Engineering, University of Shanghai for Science and Technology, Shanghai, China. [5]Jiangsu Key Laboratory of Artificial Functional Materials, Nanjing University, Nanjing, China. [6]Department of Physics, University of Arkansas, Fayetteville, AR, USA. [7]Present address: University of Southampton, Southampton, UK. [8]These authors contributed equally: Xiaoyi Xu, Tianxin Wang. ✉e-mail: zhangyong@nju.edu.cn

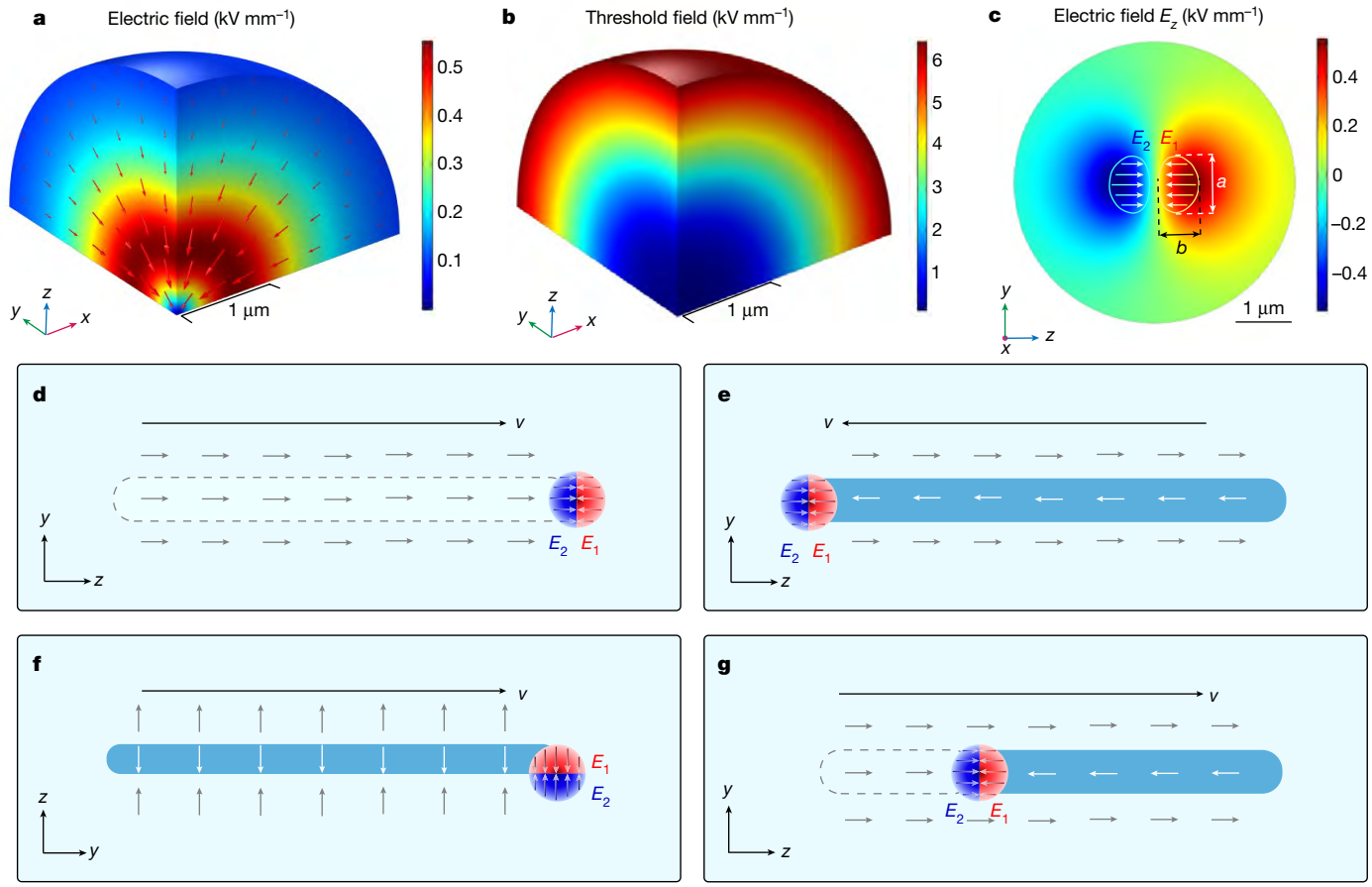

Fig. 1 | The working principle of non-reciprocal laser writing for $LiNbO_3$ ferroelectric domain engineering. a–**c**, The simulated thermoelectric field (**a**), threshold field for $LiNbO_3$ domain inversion (**b**) and the *z* component of the thermoelectric field (**c**) excited by a Gaussian laser-writing beam. The *z* components E_1 and E_2 of the thermoelectric fields (**c**) within the enclosed ellipsoidal areas (denoted by *a* and *b*) are higher than the threshold field, in which only the one antiparallel to the spontaneous polarization of $LiNbO_3$ domain can be used to pole $LiNbO_3$ domains. **d**–**g**, The principle of the non-reciprocal laser writing of $LiNbO_3$ domains, which strongly depends on the sequence of the thermoelectric fields (E_1 and E_2) applied on $LiNbO_3$ domains. When the laser beam moves along the +*z* direction, E_1 is first applied to pole the $LiNbO_3$ domain and E_2 is then applied to remove the created domain, that is, no domain structure is created at the end (**d**). When the laser-writing direction is along the −*z* direction (**e**), the sequence of E_1 and E_2 is reversed and one can laser write a domain line with a width of *a*. When the laser-writing direction is along the +*y*/−*y* direction, E_1 and E_2 separately interact with the $LiNbO_3$ domains, leading to a domain linewidth of *b* (**f**). **g**, The function of the laser eraser, in which the laser beam moves along the +*z* direction to remove the created domain.

laser spot leads to a strong head-to-head electric field at the laser spot (Fig. 1a). Second, the threshold field for $LiNbO_3$ domain inversion significantly decreases (Fig. 1b) because laser heating results in an increased ionic conductivity and therefore a reduction in domain wall pinning[51]. This makes it easier to reverse the spontaneous polarization at the laser focal point (Fig. 1c). The effective electric field above the threshold field (E_1 in Fig. 1c) is approximately an ellipsoid (denoted by *a* and *b* in Fig. 1c), which is fundamentally decided by the diffraction limit of light and the multiphoton absorption. Our theoretical simulation shows that the $LiNbO_3$ domain can be created within the area given by $a = 1$ μm and $b = 500$ nm at an input NIR light power of 130 mW (Extended Data Fig. 2 and Methods).

Notably, only the electric-field component antiparallel to the spontaneous polarization of $LiNbO_3$ crystals (E_1 in Fig. 1c) is capable of writing the ferroelectric domain structures, whereas the other electric-field components (including the component parallel to the spontaneous polarization, that is, E_2 in Fig. 1c) are not. Consequently, part of the laser-irradiated area can be spontaneous polarization inverted. The laser-writing direction determines the sequence of E_1–$LiNbO_3$-domain and E_2–$LiNbO_3$-domain interactions, which provides different functional tools for domain engineering. This is the physical origin of non-reciprocal laser writing of $LiNbO_3$ domain structures. For example, the spontaneous polarization of the $LiNbO_3$ ferroelectric domain is originally oriented along the +*z* direction. When the laser beam moves along the +*z* direction, the spontaneous polarization is first poled to the −*z* direction by E_1 and then reversed back to the +*z* direction by E_2, that is, the light–matter interactions result in finally unchanged $LiNbO_3$ domains (Fig. 1d). However, when the laser-writing direction is along the −*z* direction, the $LiNbO_3$ domain interacts with E_2 first (that is, no domain structure is created) and then is poled by E_1 (Fig. 1e). In this case, the domain-writing pencil is activated, which creates a domain line with a width of *a* (Fig. 1e). Interestingly, when moving the laser beam along the +*y* (or −*y*) direction, the effects of E_1 and E_2 are separated, and the width of the domain line becomes *b* (Fig. 1f). In addition, when moving the laser beam along an acute angle relative to the −*z* direction, one can continuously tune the domain linewidth between *a* and *b*, forming laser pencils of different diameters. This can be explained by the projection of the effective electric field in the −*z* direction (Extended Data Fig. 4).

In experiments, the first technical issue is how to laser write stable 3D domain structures inside the $LiNbO_3$ crystal. In our method, we use a high-energy laser pulse to prefabricate a drain line in the $LiNbO_3$ crystal, which is capable of effectively guiding the electric charges produced by the $LiNbO_3$ domain poling process (Methods and Extended Data Fig. 9).

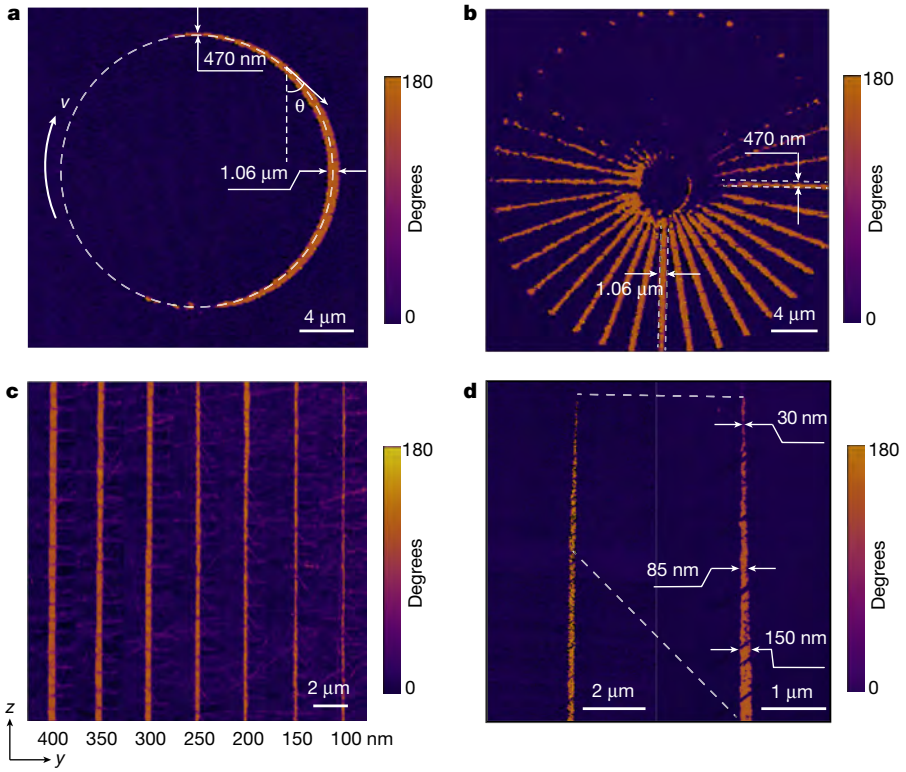

Fig. 2 | Nanoscale control of $LiNbO_3$ domains. The domain structures in the *y*–*z* plane are fabricated by using a tightly focused 800 nm laser beam and are measured by piezoresponse force microscopy (PFM, see Methods). **a**, The circle is poled by moving the laser beam clockwise. The white line indicates the laser-writing path. **b**, The radial lines are written from centre to outside. Clearly, under such a laser-writing configuration, the width of the created domain strongly depends on the laser-writing direction (defined by θ). This can be well explained by the laser–$LiNbO_3$-domain interaction mechanism described in Fig. 1. The domain widths (**a**, **b**) gradually change between around 470 nm and 1.06 μm (Extended Data Fig. 4). The NIR laser beam works well as a laser pencil of different diameters, which is restricted by the diffraction limit of light and multiphoton absorption. **c**,**d**, A laser eraser is developed to further reduce the domain linewidth far beyond the diffraction limit of light. We first laser write a domain line with a width of around 1 μm. Then, we use laser eraser to selectively remove the domain lines. **c**, The widths of the fabricated domain lines are 400 nm, 350 nm, 300 nm, 250 nm, 200 nm, 150 nm and 100 nm from left to right, respectively. **d**, A domain tip of 30 nm, which is fabricated by slightly rotating the $LiNbO_3$ sample around the *x* direction when applying the laser eraser.

Then, the low-energy laser pencil can write $LiNbO_3$ ferroelectric domain structures starting from the drain line. The $LiNbO_3$ domain structures fabricated by this method survive after being stored for two years or under annealing processes (Extended Data Fig. 7).

By use of an oil immersion objective (×63, numerical aperture = 1.4), we focus an 800 nm laser beam to pole a circle (Fig. 2a) and a radial line array (Fig. 2b) in an *x*-cut $LiNbO_3$ crystal. Here the input laser power is set to 160 mW, which is the minimal power to produce a stable $LiNbO_3$ domain structure at a depth of 30 μm in the experiment. The measured widths of the poled circle and radial line gradually change from around 470 nm to around 1.06 μm depending on the angle θ relative to the $-z$ direction (Extended Data Fig. 4), which demonstrates the functional operation of a laser pencil with different diameters. The size of the area with a *z* component of the laser-induced electric field above the

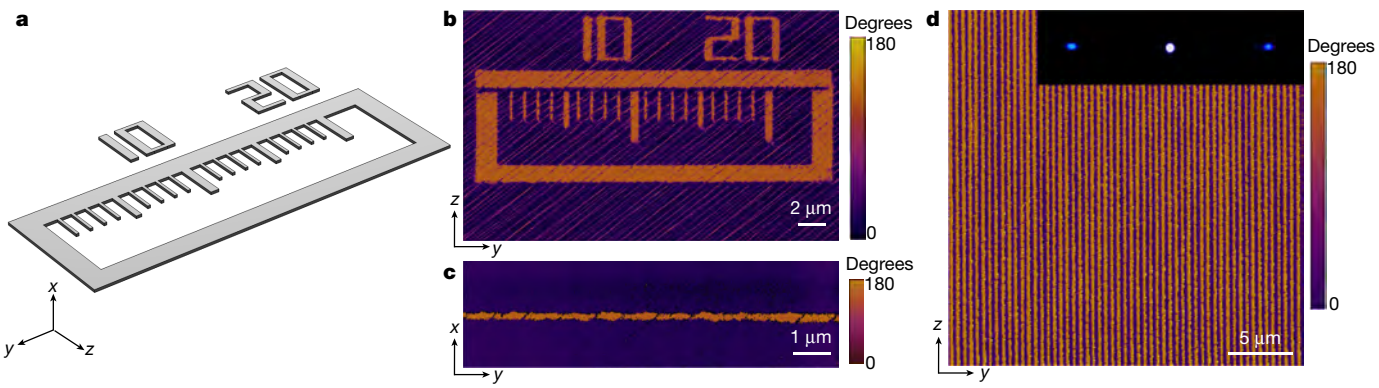

Fig. 3 | Nanodomain structure fabrication through non-reciprocal 3D laser writing. The structures are fabricated by combining the laser pencil and laser eraser and are measured by PFM. **a**, The 3D model of a ruler-shaped domain nanosheet. **b**,**c**, The cross sections of the ruler. The widths of the scale marks are 200 nm, 400 nm and 600 nm (**b**). The thickness of the ruler is 200 nm (**c**). The fabrication process is shown in Extended Data Fig. 3. **d**, A wide-angle non-linear diffraction grating. The domain linewidth is 250 nm and the period is 500 nm. The inset shows the measured non-linear Raman–Nath diffraction pattern, in which the first-order diffraction angle of the SH wave is beyond 60°.

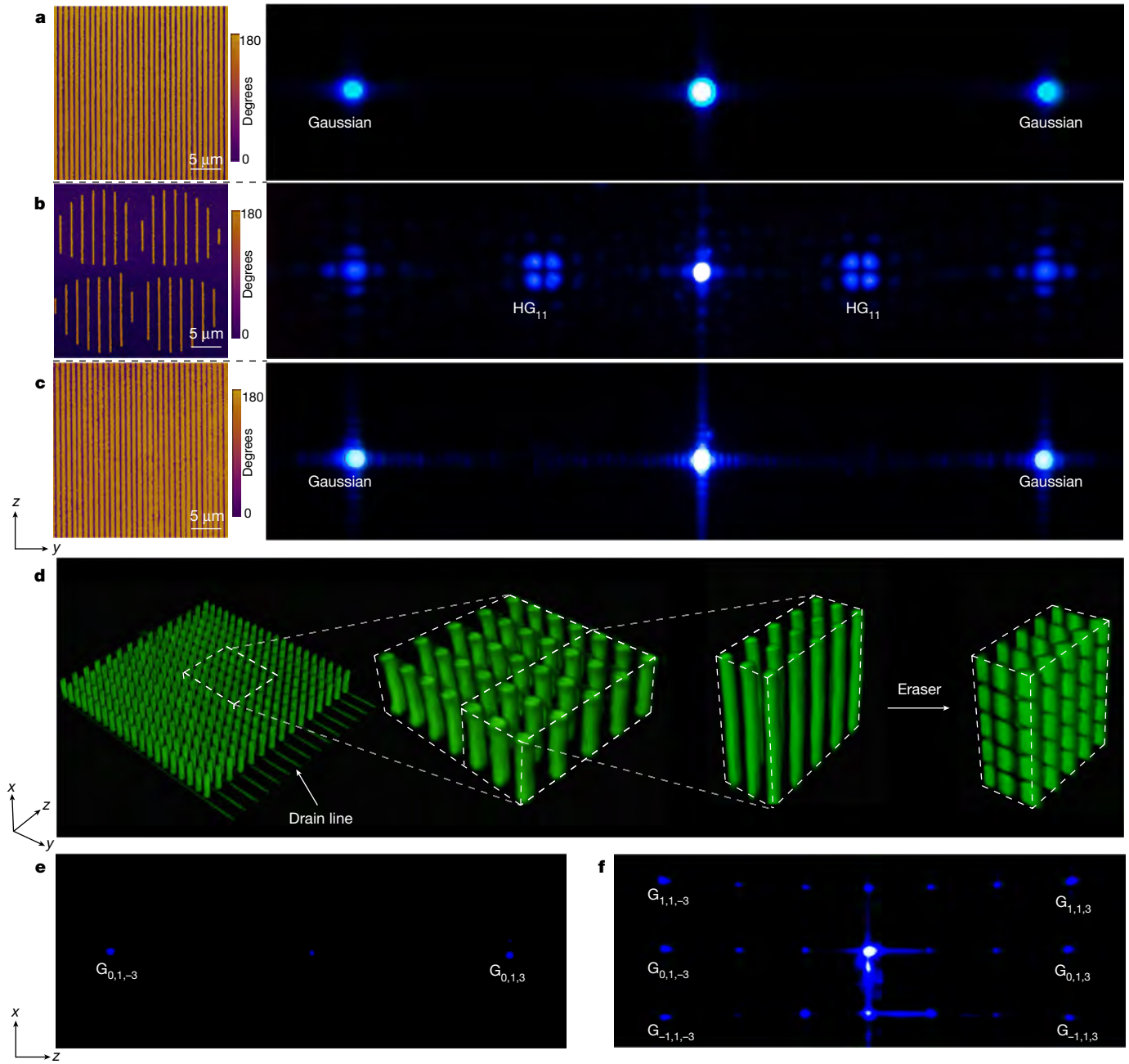

Fig. 4 | Reconfigurable $LiNbO_3$ nanodomain engineering. a–**c**, The structural conversion between two types of non-linear gratings. First, we laser write a 1D $\chi^{(2)}$ grating structure with a period of 900 nm and a linewidth of 620 nm (**a**). Then, we use the laser eraser to selectively remove the domain lines. The domain structure (**a**) is transformed into a 2D non-linear grating for SH HG-mode generation (**b**). Finally, we perform laser poling again to transform the 2D structure (**b**) back to the original 1D structure (**c**). The SH Raman–Nath diffraction patterns agree well with the domain structural conversion (**a**–**c**). In addition, the linear diffraction patterns of these gratings indicate a negligible refractive index change (Extended Data Fig. 10). **d**, A domain structure transfer from a 2D array to a 3D array, which is recorded by Cherenkov-type SH microscopy (Methods). The 2D structure is fabricated in an *x*-cut $LiNbO_3$ crystal by moving a laser beam along the +*x* direction. Then, we rotate the $LiNbO_3$ crystal by 90° along the +*z* direction. The laser beam is focused into the sample along the +*y* direction and moves along the +*z* direction to selectively remove the created domain structures. The achieved 3D domain structure has periods of $\Lambda_x = 3$ μm, $\Lambda_y = 2$ μm and $\Lambda_z = 3$ μm. The domain width is about 500 nm. Note that only a partial 3D structure is shown (**d**) owing to the view field of Cherenkov -type SH microscopy. **e**,**f**, The structure transformation (**d**) is also verified by QPM SH generation processes (Extended Data Fig. 5), through the SH patterns from 2D (**e**) and 3D (**f**) domain arrays at an input fundamental wavelength of 726 nm. Extra SH spots are present in **f** because more reciprocal vectors satisfy the QPM conditions in the 3D case (Extended Data Fig. 5).

threshold value is then deduced to be $a = 1.06$ μm and $b = 470$ nm under our experimental conditions (Fig. 1c).

To further reduce the width of the domain structures beyond the diffraction limit of light, we develop another critical tool, that is, a laser eraser, which can be used to selectively remove the previously written $LiNbO_3$ domain structures. Considering that the spontaneous polarization of the created domain structure is along the −*z* direction, this eraser function can be realized by moving the laser beam along the +*z* direction (Fig. 1g). By designing a proper strategy to combine the functions of the laser pencil and laser eraser, one can fabricate nanoscale domain structures far beyond the diffraction limit in the *x*, *y* and *z* directions (Extended Data Fig. 3). For example, Extended

Data Fig. 3a shows the process of writing a $LiNbO_3$ nanodomain line in the y–z plane. We first move the writing laser beam along the $-z$ direction to write a domain line. Then, we shift the $LiNbO_3$ sample by a designed distance d along the $+y$ (or $-y$) direction. Finally, we remove part of the created domain line by moving the laser beam back along the $+z$ direction. The width d of the remaining domain line is controlled by a piezoelectric positioner. Figure 2c shows several typical nanodomain lines with d ranging from 400 nm to 100 nm. Figure 2d shows a domain tip of 30 nm in the y–z plane. The main limit of this laser-writing strategy is currently due to the resolution of the nanopositioner and the precise control of the laser-induced electric field. Also, the depolarization effect may produce unstable domains at very thin linewidths (Methods).

Using these domain engineering tools, we have fabricated two $LiNbO_3$ nanodomain structures as examples. Figure 3a–c depicts a ruler-shaped domain nanosheet. The frames of the ruler have widths of 1.3 μm (horizontal) and 1.6 μm (vertical), which are fabricated by repeating the laser poling process. The widths of the scale marks are 200 nm, 400 nm and 600 nm, respectively, which are produced by applying the laser writing–erasing strategy with different shifting distance d. In addition, the thickness of the ruler can also be reduced down to 200 nm by a line-by-line erasing process (Fig. 3c and Extended Data Fig. 3c). Figure 3d is a wide-angle non-linear diffraction grating, which is fabricated by alternately applying the selected laser pencil and laser eraser (Extended Data Fig. 3d). The fabricated domain size is 250 nm with a period of $\Lambda = 500$ nm. According to non-linear Raman–Nath diffraction theory, the first-order diffraction angle α of the generated second harmonic (SH) wave satisfies[52]

$$\sin\alpha = \frac{\lambda_{2\omega}}{\Lambda} \tag{1}$$

where $\lambda_{2\omega}$ is the wavelength of the SH wave. At an input fundamental wavelength of 900 nm, the measured α is about 63.4°, which is consistent with the theoretical value of 64.2° (see the inset in Fig. 3d).

In particular, our method is capable of writing $LiNbO_3$ domain structures in a reconfigurable way. Figure 4 shows a conversion between different grating structures. First, we laser write a 1D $\chi^{(2)}$-grating with a period of 900 nm and a domain linewidth of 620 nm (Fig. 4a). Then, by using a laser eraser to selectively remove the domain lines, we convert the pattern into a 2D $\chi^{(2)}$-grating with a period of 1.8 μm for the generation of an SH Hermite–Gaussian (HG) beam (Fig. 4b, and see Methods for the structure design). Finally, we turn it back to the original 1D domain structure by laser rewriting the domain lines (Fig. 4c). The corresponding SH Raman–Nath diffraction patterns are shown in Fig. 4, in which the target SH beams present at the ±first diffraction order. Note that the ±first diffraction angle from the 2D $\chi^{(2)}$-grating (Fig. 4b) is half of that from 1D $\chi^{(2)}$-grating (Fig. 4a,c) because of different structure periods. These results demonstrate the ability of our method to perform high-quality reconfigurable laser-induced domain engineering.

Figure 4d gives an example of transforming a 2D domain array into a 3D array. First, we focus the laser beam along the $-x$ direction and move it along the $+x$ direction, which produces a 2D $\chi^{(2)}$-grating with a domain width of about 500 nm (see Methods for the structure fabrication). Then, we rotate the $LiNbO_3$ sample by an angle of 90° around the $+z$ direction. Finally, the laser beam is focused along the $+y$ direction and moves along the $+z$ direction to selectively remove the created domain lines. Figure 4d shows the Cherenkov-type SH microscopic images of the fabricated 2D and 3D non-linear grating structures (Methods). We also use QPM SH generations to demonstrate the successful transformation from 2D to 3D modulation of $\chi^{(2)}$ (Fig. 4e,f). The QPM condition of an SH generation process can be written as

$$\boldsymbol{k}_{2\omega} - 2\boldsymbol{k}_{\omega} - \boldsymbol{G}_{m,n,l} = 0 \tag{2}$$

where $\boldsymbol{k}_{\omega}$ and $\boldsymbol{k}_{2\omega}$ are the wave vectors of the fundamental and SH waves, respectively. The reciprocal vector $\boldsymbol{G}_{m,n,l}$ is defined as

$$\boldsymbol{G}_{m,n,l} = m\frac{2\pi}{\Lambda_x}\hat{\mathbf{x}} + n\frac{2\pi}{\Lambda_y}\hat{\mathbf{y}} + l\frac{2\pi}{\Lambda_z}\hat{\mathbf{z}} \tag{3}$$

where Λ_x, Λ_y and Λ_z are the structure periods along the x, y and z directions, respectively. The QPM wavelengths are experimentally measured by scanning the fundamental wavelength (Extended Data Fig. 5). Figures 4e,f compare the experimental SH patterns from 2D and 3D domain arrays at a fundamental wavelength of 726 nm. Clearly, in comparison to the 2D case (Fig. 4e), more reciprocal vectors in the 3D structure satisfy the QPM condition, which results in extra SH spots (Fig. 4f). In addition, a similar laser-writing strategy is applied to convert a 2D non-linear grating into a 3D HG-mode non-linear grating (Extended Data Fig. 6).

Summary and outlook

In this article, we propose and experimentally demonstrate a non-reciprocal femtosecond laser-writing technique for reconfigurable 3D nanoscale ferroelectric domain engineering in $LiNbO_3$ crystals. By properly designing the fabrication strategy to fully utilize the functionalities of the developed laser pencil and laser eraser, one can fabricate arbitrary 3D ferroelectric domain structures with features beyond state of the art. For example, the resolution of $LiNbO_3$ domain engineering is significantly reduced down to 30 nm, which is mainly limited by the system performance and the depolarization mechanism (Methods). The non-reciprocity of our laser-writing technique also provides a critical tool to re-write $LiNbO_3$ domain structures. High-resolution reconfigurable manipulation of $LiNbO_3$ ferroelectric domains can significantly enhance the ability to control non-linear optical interactions for high-efficiency frequency conversion[11,20] and narrow-linewidth quantum entanglement generation[24]. In addition to optics, the developed nanodomain-engineering technique also paves the way to achieve high-performance ferroelectric-domain-wall-based nanoelectronic devices such as high-capacity rewritable non-volatile memories[19,22]. Additionally, one can fabricate nanosized $LiNbO_3$ domain arrays to compose high-frequency acoustic resonators and filters over 10 GHz (Extended Data Fig. 8). Such new nanodomain-engineering techniques can be further applied in other ferroelectric crystals, including lithium tantalate and potassium titanyl phosphate, which can boost the developments of high-quality 3D integrated nanodevices for advanced photonic, electronic and phononic applications.

Online content

Any methods, additional references, Nature Research reporting summaries, source data, extended data, supplementary information, acknowledgements, peer review information; details of author contributions and competing interests; and statements of data and code availability are available at https://doi.org/10.1038/s41586-022-05042-z.

1. Zhu, D. et al. Integrated photonics on thin-film lithium niobate. *Adv. Opt. Photon.* **13**, 242–352 (2021).
2. Sun, D. H. et al. Microstructure and domain engineering of lithium niobate crystal films for integrated photonic applications. *Light Sci. Appl.* **9**, 197 (2020).
3. Wang, C. et al. Integrated lithium niobate electro-optic modulators operating at CMOS-compatible voltages. *Nature* **562**, 101–104 (2018).
4. He, M. B. et al. High-performance hybrid silicon and lithium niobate Mach-Zehnder modulators for 100 Gbit s^{-1} and beyond. *Nat. Photon.* **13**, 359–365 (2019).
5. Li, M. X. et al. Lithium niobate photonic-crystal electro-optic modulator. *Nat. Commun.* **11**, 4123 (2020).
6. Zhang, M. et al. Broadband electro-optic frequency comb generation in a lithium niobate microring resonator. *Nature* **568**, 373–377 (2019).
7. He, Y. et al. Self-starting bi-chromatic $LiNbO_3$ soliton microcomb. *Optica* **6**, 1138–1144 (2019).

8. Pohl, D. et al. An integrated broadband spectrometer on thin-film lithium niobate. *Nat. Photon.* **14**, 24–29 (2019).
9. Bartnick, M. et al. Cryogenic second-harmonic generation in periodically poled lithium niobate waveguides. *Phys. Rev. Appl.* **15**, 024028 (2021).
10. Jankowski, M. et al. Ultrabroadband nonlinear optics in nanophotonic periodically poled lithium niobate waveguides. *Optica* **7**, 40–46 (2020).
11. Zhu, S. N., Zhu, Y. Y. & Ming, N. B. Quasi–phase-matched third-harmonic generation in a quasi-periodic optical superlattice. *Science* **278**, 843–846 (1997).
12. Ellenbogen, T., Noa, V. B., Ayelet, G. P. & Arie, A. Nonlinear generation and manipulation of Airy beams. *Nat. Photon.* **3**, 395–398 (2009).
13. Yuan, S. et al. Strongly enhanced second harmonic generation in a thin film lithium niobate heterostructure cavity. *Phys. Rev. Lett.* **127**, 153901 (2021).
14. Yudistira, D., Benchabane, S., Janner, D. & Pruneri, V. Diffraction less and strongly confined surface acoustic waves in domain inverted $LiNbO_3$ superlattices. *Appl. Phys. Lett.* **98**, 233504 (2011).
15. Yin, R. C., Yu, S. Y., He, C., Lu, M. H. & Chen, Y. F. Bulk acoustic wave delay line in acoustic superlattice. *Appl. Phys. Lett.* **97**, 092905 (2010).
16. Yudistira, D., Benchabane, S., Janner, D. & Pruneri, V. Surface acoustic wave generation in *zx*-cut $LiNbO_3$ superlattices using coplanar electrodes. *Appl. Phys. Lett.* **95**, 052901 (2009).
17. Lu, Y. Q. et al. Optical properties of an ionic-type phononic crystal. *Science* **284**, 1822–1824 (1999).
18. Chai, X. et al. Nonvolatile ferroelectric field-effect transistors. *Nat. Commun.* **11**, 2811 (2020).
19. Meier, D. & Selbach, S. M. Ferroelectric domain walls for nanotechnology. *Nat. Rev. Mater.* **7**, 157–173 (2021).
20. Canalias, C. & Pasiskevicius, V. Mirrorless optical parametric oscillator. *Nat. Photon.* **1**, 459–462 (2007).
21. Jia, K. P. et al. Midinfrared tunable laser with noncritical frequency matching in box resonator geometry. *Phys. Rev. Lett.* **127**, 213902 (2021).
22. Sharma, P. et al. Nonvolatile ferroelectric domain wall memory. *Sci. Adv.* **3**, 1700512 (2017).
23. Marpaung, D., Yao, J. P. & Capmany, J. Integrated microwave photonics. *Nat. Photon.* **13**, 80–90 (2019).
24. Jin, H. et al. On-chip generation and manipulation of entangled photons based on reconfigurable lithium-niobate waveguide circuits. *Phys. Rev. Lett.* **113**, 103601 (2014).
25. Solntsev, A. S. et al. Generation of nonclassical biphoton states through cascaded quantum walks on a nonlinear chip. *Phys. Rev. X* **4**, 031007 (2014).
26. Saravi, S., Pertsch, T. & Setzpfandt, F. Lithium niobate on insulator: An emerging platform for integrated quantum photonics. *Adv. Opt. Mater.* **9**, 2100789 (2021).
27. Zhao, J., Ma, C., Rusing, M. & Mookherjea, S. High quality entangled photon pair generation in periodically poled thin-film lithium niobate waveguides. *Phys. Rev. Lett.* **124**, 163603 (2020).
28. Lehr, D. et al. Enhancing second harmonic generation in gold nanoring resonators filled with lithium niobate. *Nano Lett.* **15**, 1025–1030 (2015).
29. Wang, J. et al. High-Q lithium niobate microdisk resonators on a chip for efficient electro-optic modulation. *Opt. Express* **23**, 23072–23078 (2015).
30. Shur, V. Y., Akhmatkhanov, A. R. & Baturin, I. S. Micro- and nano-domain engineering in lithium niobate. *Appl. Phys. Lett.* **2**, 040604 (2015).
31. Ying, C. Y. J. et al. Light-mediated ferroelectric domain engineering and micro-structuring of lithium niobate crystals. *Laser Photonics Rev.* **6**, 526–548 (2012).
32. Sun, J., Hao, Y. X., Zhang, L., Xu, J. J. & Zhu, S. N. Brief review of lithium niobate crystal and its applications. *J. Synth. Cryst.* **49**, 947–964 (2020).
33. Armstrong, J. A., Bloembergen, N., Ducuing, J. & Pershan, P. S. Interactions between light waves in a nonlinear dielectric. *Phys. Rev.* **127**, 1918–1939 (1962).
34. Cao, B. et al. Efficient generation of ultra-broadband parametric fluorescence using chirped quasi-phase-matched waveguide devices. *Opt. Express* **29**, 21615–21628 (2021).
35. Yudistira, D., Janner, D., Benchabane, S. & Pruneri, V. Low power consumption integrated acoustooptic filter in domain inverted $LiNbO_3$ superlattice. *Opt. Express* **18**, 27181–27190 (2010).
36. Rosenman, G., Urenski, P., Agronin, A., Rosenwaks, Y. & Molotskii, M. Submicron ferroelectric domain structures tailored by high-voltage scanning probe microscopy. *Appl. Phys. Lett.* **82**, 103–105 (2003).
37. Yamada, M. & Kishima, K. Fabrication of periodically reversed domain structure for SHG in $LiNbO_3$ by direct electron beam lithography at room temperature. *Electron. Lett.* **27**, 828–829 (1991).
38. Shur, V. Y. Domain nanotechnology in ferroelectrics: nano-domain engineering in lithium niobate crystals. *Ferroelectrics* **373**, 1–10 (2010).
39. Shur, V. Y. et al. Self-assembled shape evolution of the domain wall and formation of nanodomain wall traces induced by multiple IR laser pulse irradiation in lithium niobate. *J. Appl. Phys.* **127**, 094103 (2020).
40. Shur, V. Y. et al. Dimensionality increase of ferroelectric domain shape by pulse laser irradiation. *Acta Mater.* **219**, 117270 (2021).
41. Rodenas, A. et al. Three-dimensional femtosecond laser nanolithography of crystals. *Nat. Photon.* **13**, 105–109 (2018).
42. Gattass, R. R. & Mazur, E. Femtosecond laser micromachining in transparent materials. *Nat. Photon.* **2**, 219–225 (2008).
43. Huang, X. J. et al. Reversible 3D laser printing of perovskite quantum dots inside a transparent medium. *Nat. Photon.* **14**, 82–88 (2019).
44. Yang, W., Kazansky, P. G. & Svirko, Y. P. Non-reciprocal ultrafast laser writing. *Nat. Photon.* **2**, 99–104 (2008).
45. Wei, D. Z. et al. Experimental demonstration of a three-dimensional lithium niobate nonlinear photonic crystal. *Nat. Photon.* **12**, 596–601 (2018).
46. Xu, T. X. et al. Three-dimensional nonlinear photonic crystal in ferroelectric barium calcium titanate. *Nat. Photon.* **12**, 591–595 (2018).
47. Chen, X. et al. Ferroelectric domain engineering by focused infrared femtosecond pulses. *Appl. Phys. Lett.* **107**, 141102 (2015).
48. Imbrock, J., Hanafi, H., Ayoub, M. & Denz, C. Local domain inversion in MgO-doped lithium niobate by pyroelectric field-assisted femtosecond laser lithography. *Appl. Phys. Lett.* **113**, 252901 (2018).
49. Zhang, Y., Sheng, Y., Zhu, S. N., Xiao, M. & Krolikowski, W. Nonlinear photonic crystals: from 2D to 3D. *Optica* **8**, 372–381 (2021).
50. Zhu, B., Liu, H., Chen, Y. & Chen, X. High conversion efficiency second-harmonic beam shaping via amplitude-type nonlinear photonic crystals. *Opt. Lett.* **45**, 220–223 (2019).
51. Steigerwald, H., Cube, F. V., Luedtke, F., Dierolf, V. & Buse, K. Influence of heat and UV light on the coercive field of lithium niobate crystals. *Appl. Phys. B* **101**, 535–539 (2010).
52. Saltiel, S. M. et al. Nonlinear diffraction from a virtual beam. *Phys. Rev. Lett.* **104**, 083902 (2010).

Methods

Experimental set-up of non-reciprocal laser writing

A femtosecond laser-writing system is used to fabricate 3D nanodomain structures in 5% MgO-doped *x*-cut $LiNbO_3$ crystals, as shown in Extended Data Fig. 1. The light source is output from a mode-locked Ti:sapphire laser (Chameleon Vision-S, Coherent), which works at an 800 nm wavelength, a 75 fs pulse duration and an 80 MHz pulse repetition rate. The laser passes through a beam expander (consisting of two lenses with focal lengths of 50 mm and 150 mm) and a shutter. Then, it is focused into $LiNbO_3$ crystals by an oil immersion objective (×63, numerical aperture = 1.4). The $LiNbO_3$ sample is mounted on a nanopositioning stage (P562.6, Physik Instrument), which has a range of 200 μm (*x*) × 200 μm (*y*) × 200 μm (*z*) and an accuracy of 5 nm. The fabrication process can be monitored by a charge-coupled device in real time. The scanning speed is 10 μm s^{-1}. At a depth of 30 μm, the input laser power is 160 mW (corresponding to a pulse energy of 2 nJ) to fabricate $LiNbO_3$ domain structures. To fabricate a drain line, the laser power is 200 mW (corresponding to a pulse energy of 2.5 nJ). Note that the optimal experiment parameters vary with the fabrication depth.

Pulse energy compensation to fabricate a domain line along the depth direction

When a focused wave front converges from air into $LiNbO_3$ crystal, strong spherical aberration will distort the focal intensity distribution because of refractive index mismatch. For instance, the axial length of the focal spot (along the *x* direction in our case) increases appreciably with the fabrication depth, leading to a decrease of the peak intensity. In this work, we optimize the pulse energies at different depths to compensate for the effect of spherical aberration. The ratios of the pulse energies (normalized to the value at a depth of 30 μm) are 1.25, 1.55 and 1.85 when increasing the depth to 45 μm, 60 μm, and 75 μm, respectively. In the experiment, we use this strategy to fabricate a 2D domain array consisting of 50-μm-long domain lines (Fig. 4d). By gradually polishing the sample and performing PFM measurements, we obtain the standard deviation of the domain size to be 38 nm, which can be mainly attributed to the residual distortion of the focused laser spot at different depths.

The laser-induced electric-field theory

The absorption band edge of 5% MgO-doped $LiNbO_3$ crystal is 318 nm (ref. [53]). Three-photon absorption dominates the light–matter interaction under the illumination of an 800 nm laser beam[54]. The laser-induced local temperature field leads to the generation of an electric field (due to the $LiNbO_3$ thermoelectric[55,56] and pyroelectric effects[57]) and a reduced threshold field[51] for $LiNbO_3$ domain poling (owing to the increased local temperature).

Our laser-writing process can be divided into three phases. The pyroelectric effect (depending on the time-varying temperature) and the thermoelectric effect (resulting from the temperature gradient) play the dominant roles in different phases. In phase 1, the NIR light is tightly focused onto a certain point close to the prefabricated drain line, which leads to a local heating process. Considering the high power density in our experiment, the local temperature rapidly increases, resulting in a high pyroelectric field that could pole the domain at the starting point. In phase 2, the temperature field reaches a thermodynamic equilibrium, which depends on the power and profile of the input laser and the heat conduction of the $LiNbO_3$ crystal. The steep temperature gradient (due to the tightly focused laser spot) produces a strong thermoelectric field. In phase 3, we move the laser beam inside the $LiNbO_3$ crystal, which is equivalent to moving the temperature field along with the laser-writing beam. Considering the laser-writing speed and the temperature gradient, the pyroelectric field in this phase (Extended Data Fig. 2d) is about one order of magnitude smaller than the thermoelectric field (Extended Data Fig. 2c), that is, the thermoelectric field is the dominant effect in the domain-writing process under our experimental conditions.

Next, we numerically simulate the thermoelectric field to write domain structures. We assume that the focused light field has a Gaussian profile, which can be written as

$$\mathrm{I} = I_0 G(x, y, z) \tag{4}$$

where I_0 is the power of the incident laser and $G(x, y, z)$ is a 3D Gaussian function. Three-photon absorption produces a temperature field near the focal point, that is,

$$\mathrm{Q} = \gamma I^3 \tag{5}$$

Here γ is the three-photon absorption coefficient of the $LiNbO_3$ crystal and Q is the heat energy. Consider a solid heat transfer model in the $LiNbO_3$ crystal, that is,

$$\rho C_\mathrm{p} \nabla T \mathbf{u} - \kappa \nabla^2 T = Q \tag{6}$$

where C_p is the heat capacity, ρ is the crystal density, κ is the thermal conductivity, T is the temperature and $\mathbf{u}$ is the velocity vector. The temperature gradient causes a potential difference between the cold side and the hot side of the laser-illuminated area, leading to an electric field of

$$E = S\Delta T \tag{7}$$

where S is the Seebeck coefficient. Above room temperature[58], the threshold field for $LiNbO_3$ domain poling decreases with increasing temperature[51,59,60]. In our simulations, the parameters[54,56,59] are $C_\mathrm{p} = 619\mathrm{J{\bullet}kg^{-1}{\bullet}K^{-1}}$, $\rho = 4648\mathrm{kg{\bullet}m^{-3}}$, $\kappa = 5.6\mathrm{W{\bullet}m^{-1}{\bullet}K^{-1}}$, $\mathrm{S} = 10^{-3}\mathrm{V{\bullet}K^{-1}}$, $\gamma = 10^{-15}\ \mathrm{m^3{\bullet}W^{-2}}$, $I_0 = 0.13\mathrm{W}$ and the full-width half-maximum of $G(x, y, z)$ is set to 2 μm. The calculated temperature field and temperature gradient are given in Extended Data Fig. 2a and b, respectively. Note that only the z component of the electric field (E_z) is used for $LiNbO_3$ domain engineering. The calculated E_z is shown in Extended Data Fig. 2c, in which the enclosed regions indicate its value above the threshold field.

Designing $LiNbO_3$ domain structures for non-linear beam shaping

$LiNbO_3$ domain structure with a certain $\chi^{(2)}$ distribution can be used to shape the wave front of the SH beam. We first consider a 2D domain structure. On the basis of binary computer-generated-hologram theory[61], the 2D structure function to produce a target SH beam is given by[62]

$$f(y, z) = T\{\cos[G_y y - \arg(E_{2\omega})] - \cos[\sin^{-1}\mathrm{amp}(E_{2\omega})]\} \tag{8}$$

Here $E_{2\omega} = E_{2\omega}(y, z)$ is the target SH beam, G_y is the spatial frequency along the *y* direction. arg and amp represent the phase and amplitude of $E_{2\omega}$, respectively. The function T is defined as

$$T(X) = \begin{cases} 1, X \geq 0 \\ -1, X < 0 \end{cases} \tag{9}$$

The distribution of $\chi^{(2)}$ is

$$\chi^{(2)}(y, z) = -d_{33} f(y, z) \tag{10}$$

with d_{33} being the $LiNbO_3$ non-linear coefficient used in our experiment.

We design a structure to generate an SH HG beam for example, which is written as[63]

$$E_{2\omega}^{p,q}(y,z) = H_p\left(\sqrt{2}\frac{y}{w_0}\right)\exp\left(-\frac{y^2}{w_0^2}\right)H_q\left(\sqrt{2}\frac{z}{w_0}\right)\exp\left(-\frac{z^2}{w_0^2}\right) \quad (11)$$

Here, w_0 is the waist of the HG beam, and $H_p\left(\sqrt{2}\frac{y}{w_0}\right)$ and $H_q\left(\sqrt{2}\frac{z}{w_0}\right)$ are the pth- and qth-order Hermite polynomials, respectively. The structure function for the SH HG_{00} beam (that is, the SH Gaussian beam) generation is a 1D grating of

$$f_{HG_{00}}(y,z) = T\{\cos(G_y^{00}y)\} \quad (12)$$

To produce an SH HG_{11} beam of

$$E_{2\omega}^{1,1}(y,z) = \frac{8yz}{w_0^2}\exp\left(-\frac{y^2}{w_0^2}\right)\exp\left(-\frac{z^2}{w_0^2}\right) \quad (13)$$

the 2D structure function can be expressed as

$$f_{HG_{11}}(y,z) = T\{\cos[G_y^{11}y - \arg(E_{2\omega}^{11})] - \cos[\sin^{-1}\mathrm{amp}(E_{2\omega}^{11})]\} \quad (14)$$

By using the above configuration, the target SH beam presents at the first diffraction order.

When designing 3D domain structure for the SH HG_{11} beam generation under 3D QPM conditions, the domain structure in the y–z plane is also defined by equation (14), which is periodically arranged along the x direction (Extended Data Fig. 6a). In our experiment, the periods are 2 μm and 6 μm along the x and z directions, respectively. We measure the SH power at different fundamental wavelengths (Extended Data Fig. 6b). The pump power is kept at 1.5 W. The output SH power reaches its maximum at a fundamental wavelength of 768 nm, that is, 3D QPM is fully satisfied.

PFM image of $LiNbO_3$ ferroelectric domains

PFM uses a standard scanning force microscopy operated in contact mode[64]. When an additional driving voltage is applied to the conductive tip, the ferroelectric domain structure leads to deflection, buckling and torsion of the cantilever. Here deflection is related to the out-of-plane PFM signal, whereas buckling and torsion are related to the in-plane PFM signal. The difference between PFM signals can be used to distinguish various ferroelectric domains. In the experiment, the sample is polished to bring the domain structures to the surface before performing the PFM measurement. The driving voltage is 1 V. The contact resonance frequencies are 350 kHz and 660 kHz for the out-of-plane mode and in-plane mode, respectively.

3D Cherenkov SH image of $LiNbO_3$ ferroelectric domains

Because the Cherenkov SH signal is greatly enhanced at the ferroelectric domain walls[65,66], it is used to visualize the $LiNbO_3$ domain structures. The Cherenkov SH wave emits at an angle θ satisfying $\cos\theta = 2k_1/k_2$, where k_1 and k_2 denote the wave vectors of the fundamental and SH waves, respectively. In the experiment, we build a Cherenkov-type SH microscope. The wavelength of the fundamental wave is 900 nm. After filtering out the fundamental wave and collinear SH wave, we record the Cherenkov SH signals by scanning the $LiNbO_3$ sample point by point, to compose a 3D image of the $LiNbO_3$ domain structure.

Experimental limits to fabricate $LiNbO_3$ nanodomains

To reduce the domain linewidth below the diffraction limit, we have developed a laser eraser to selectively remove the previously written domains. The fabrication strategy is shown in Extended Data Fig. 3. The domain quality in this technique strongly depends on the precision and stability of the laser-writing system. In our experiment, the resolution of the nanopositioner used is 5 nm. The power fluctuation of the femtosecond laser is 0.5%, which causes an estimated variation of 5 nm in the laser-induced electric field above the threshold. In addition, the PFM measurement has a resolution of 5 nm. Under such experimental conditions, the overall fluctuation in the recorded domain linewidth is estimated to be 15 nm.

When approaching the experimental limit of the $LiNbO_3$ nanodomain linewidth, the depolarization field could cause non-ideal and unstable domain structures. In addition, when fabricating a $LiNbO_3$ nanodomain grating, the possible degradation of the polarization driven by the remaining charges in the neighbouring domains could make it difficult to realize high-quality domain gratings of very small periods. Under our present experimental conditions, the remaining charges in the neighbouring domains may interact with each other when the period is below 500 nm. The laser-writing parameters need to be carefully optimized to further improve $LiNbO_3$ nanodomain quality.

Data availability

Source data for Extended Data Figs. 4b and 6b are provided with the paper. The data supporting the findings of this study are available within the article.

53. Bhatt, R. et al. Studies on nonlinear optical properties of ferroelectric MgO-$LiNbO_3$ single crystals. *Ferroelectrics* **323**, 165–169 (2005).
54. Reddy, J. N. B., Elizabeth, S., Bhat, H. L., Venkatram, N. & Rao, D. N. Influence of non-stoichiometric defects on nonlinear absorption and refraction in Nd:Zn co-doped lithium niobate. *Opt. Mater.* **31**, 1022–1026 (2009).
55. Maekawa, S. et al. in *Physics of Transition Metal Oxides* (eds Cardona, M. et al.) 323–331 (Springer, 2004).
56. Ashcroft, N. W. & Mermin, N. D. in *Solid State Physics* (ed. Crane, D. G.) 253–258 (Harcourt College, 1976).
57. Kosorotov, V. F., Kremenchugskij, L. S., Levash, L. V. & Shchedrina, L. V. Tertiary pyroelectric effect in lithium niobate and lithium tantalate crystals. *Ferroelectrics* **70**, 27–37 (1986).
58. Bo, H. F. et al. Temperature-dependent ferroelectric properties of near stoichiometric lithium niobate single crystal. *Appl. Phys. A* **124**, 691 (2018).
59. Fridkin, V. M. & Ducharme, S. General features of the intrinsic ferroelectric coercive field. *Phys. Solid State* **43**, 1320–1324 (2001).
60. Ishizuki, H., Shoji, I. & Taira, T. Periodical poling characteristics of congruent MgO:$LiNbO_3$ crystals at elevated temperature. *Appl. Phys. Lett.* **82**, 4062–4064 (2003).
61. Lee, W. H. Binary computer-generated holograms. *Appl. Opt.* **18**, 3661–3669 (1979).
62. Shapira, A., Shiloh, R., Juwiler, I. & Arie, A. Two-dimensional nonlinear beam shaping. *Opt. Lett.* **37**, 2136–2138 (2012).
63. Kogelnik, H. & Li, T. Laser beams and resonators. *Appl. Opt.* **5**, 1550–1567 (1966).
64. Soergel, E. Piezoresponse force microscopy (PFM). *J. Phys. D* **44**, 464003 (2011).
65. Sheng, Y. et al. Three-dimensional ferroelectric domain visualization by Čerenkov-type second harmonic generation. *Opt. Express* **18**, 16539–16545 (2010).
66. Huang, X. Y. et al. Second-harmonic interference imaging of ferroelectric domains through a scanning microscope. *J. Phys. D* **50**, 485105 (2017).
67. Zhu, Y. Y., Chen, Y. F., Zhu, S. N., Qin, Y. Q. & Ming, N. B. Acoustic superlattices and ultrasonic waves excited by crossed-field scheme. *Mater. Lett.* **28**, 503–505 (1996).
68. Anhorn, M., Engan, H. E. & Ronnekleiv, A. New saw velocity measurements on y-cut $LiNbO_3$. *In IEEE 1987 Ultrasonics Symposium* (ed. McAvoy, B. R.) 279–284 (IEEE, 1987).

Acknowledgements This work was supported by the National Key R&D Programme of China (grant nos. 2021YFA1400803 and 2017YFA0303703), the National Natural Science Foundation of China (NSFC) (grant nos. 91950206, 92163216, 11874213, 51725203, U1932115, 51721001 and 62005164), the Science and Technology Commission of Shanghai Municipality (grant no. 21DZ1100500), the Shanghai Municipal Science and Technology Major Project, the Shanghai Frontiers Science Centre Programme (grant no. 2021-2025 No. 20), the Zhangjiang National Innovation Demonstration Zone (grant no. ZJ2019-ZD-005), the Shanghai Rising-Star Program (grant no. 20QA1404100), the National Key Scientific Instrument and Equipment Development Project (grant no. 61927814) and the Fundamental Research Funds for the Central Universities (grant no. 021314380191).

Author contributions Y.Z. conceived the idea and supervised the project with M.X. X.X., T.W., P.C., C.Z, J.M., D. Wei, H.W., B.N. and X.F. performed the experiments and numerical simulations under the guidance of Y.Z., S.Z., D. Wu, M.G. and M.X. All authors contributed to the discussion of experimental results.

Competing interests The authors declare no competing interests.

Additional information

Supplementary information The online version contains supplementary material available at https://doi.org/10.1038/s41586-022-05042-z.

Correspondence and requests for materials should be addressed to Yong Zhang.

Peer review information *Nature* thanks Airán Ródenas Seguí and the other, anonymous, reviewer(s) for their contribution to the peer review of this work.

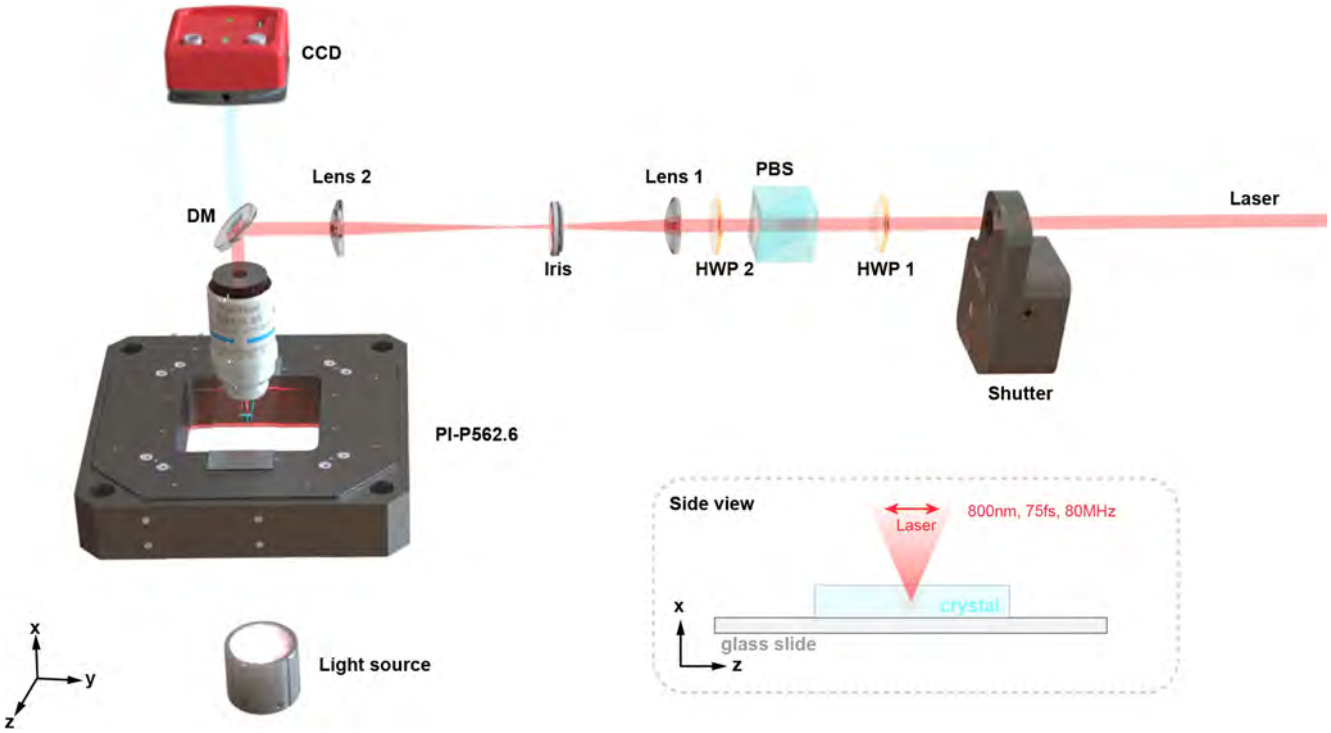

Extended Data Fig. 1 | Femtosecond laser writing system for $LiNbO_3$ nanodomain engineering. The *z*-polarized laser beam is focused into the sample along the *x* direction.

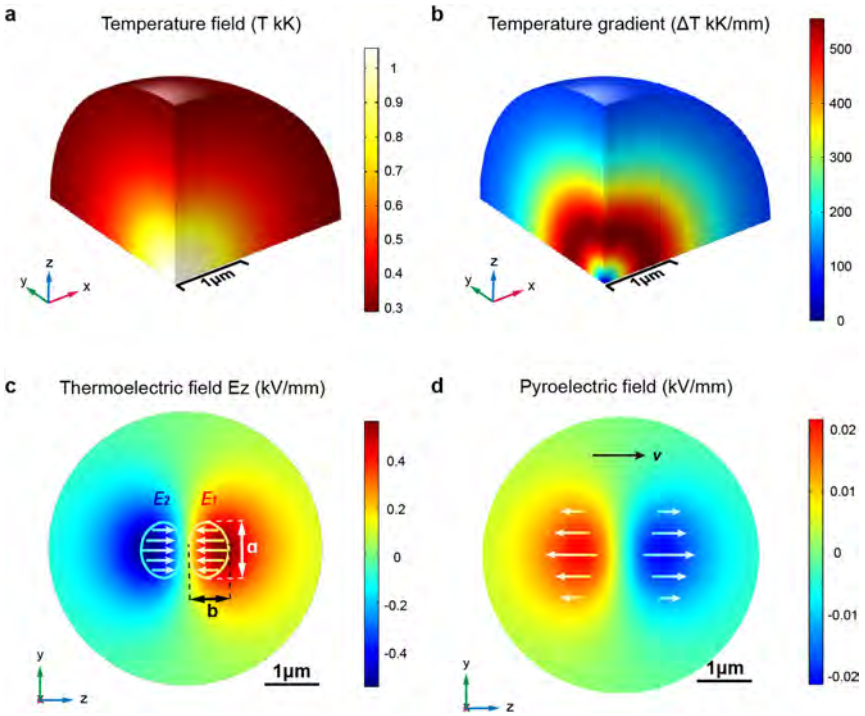

Extended Data Fig. 2 | The theoretical simulation of temperature (a), temperature gradient (b), the *z*-component of the thermoelectric field (c), and the pyroelectric field (d). The marked area in **c** indicates the electric field above the threshold value. In **d**, the black arrow shows the laser writing direction (v = 10 μm/s) and the white arrows indicate the direction of pyroelectric field. The input laser propagates along the *x* direction with its polarization along the *z* direction.

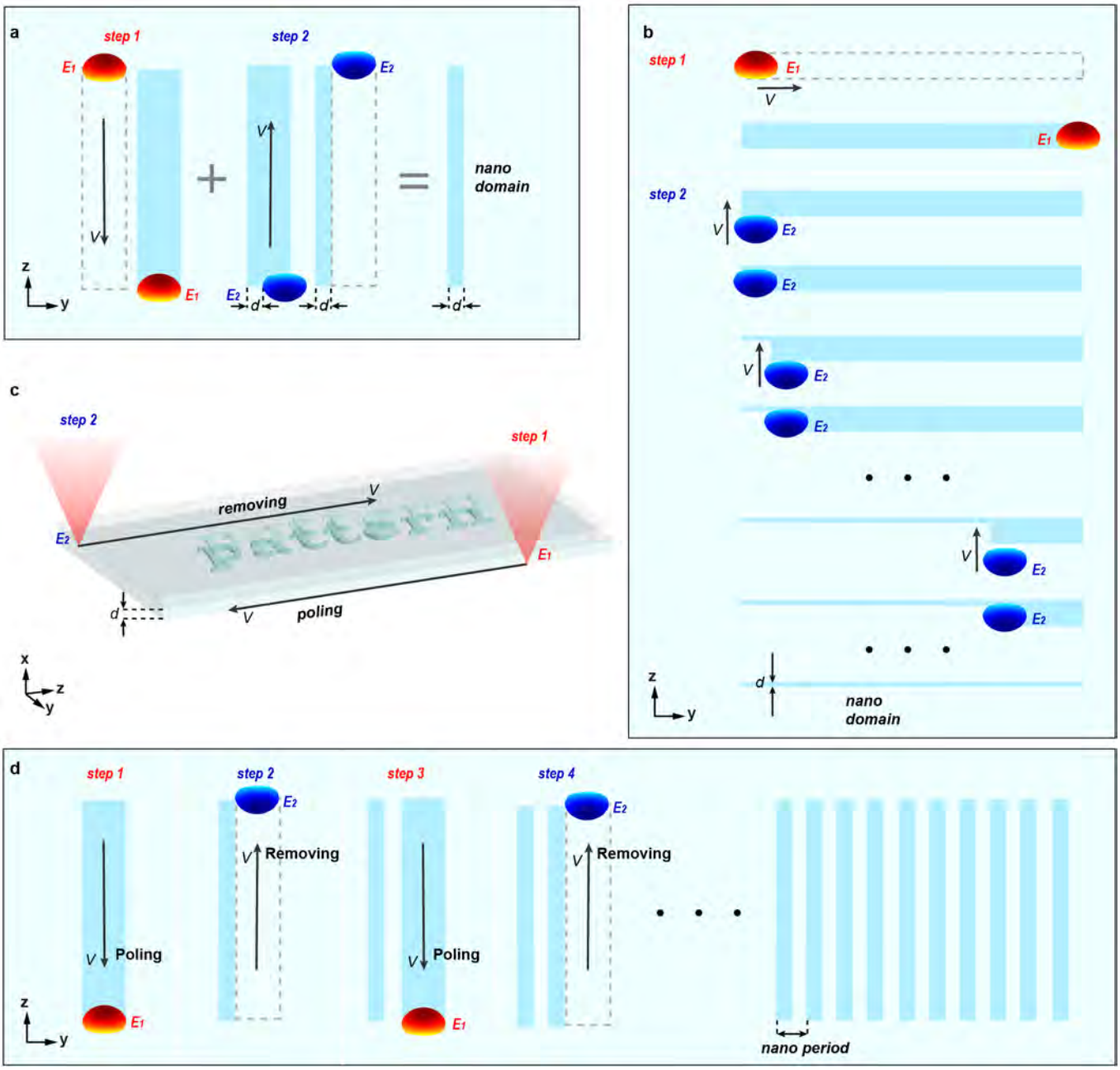

Extended Data Fig. 3 | The procedures to fabricate nanodomains along the *x*, *y*, and *z* directions, through laser poling-erasing strategy. a, The laser writing process to fabricate $LiNbO_3$ nanodomains along the *y* direction. First, we move the laser beam along the $-z$ direction to write a domain line. Then, we shift the $LiNbO_3$ sample by a designed distance *d* along the $+y$ (or $-y$) direction. Finally, we remove part of the created domain by moving the laser beam back along the $+z$ direction. The remaining domain width along the *y* direction is *d* (**a**). By shifting the $LiNbO_3$ sample along the *x* direction, similar laser writing strategy is applied to reduce the domain linewidth along the *x* direction (**c**). **b**, The procedure to produce nanosized domain along the *z* direction, we first move the laser beam along the *y* direction to write a domain line. Then, we apply the laser eraser point by point to reduce the domain width along the *z* direction. **d**, The fabrication process of a nanodomain array.

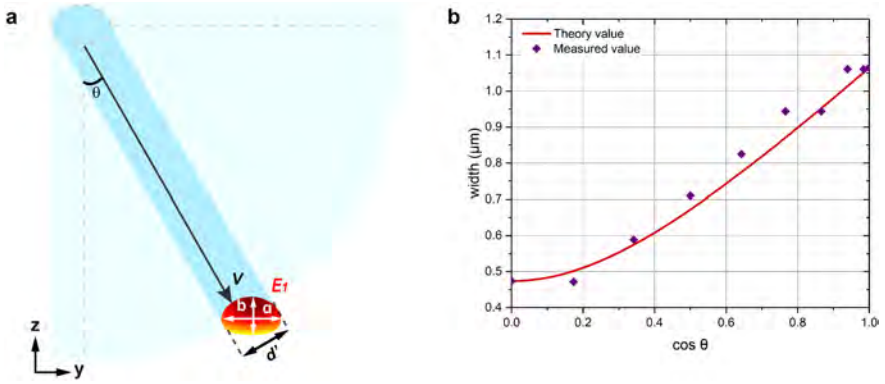

Extended Data Fig. 4 | The dependence of domain width on the writing direction. a, Schematic diagram of laser writing along an angle of θ relative to the -*z* direction. *a* and *b* define the effective thermoelectric field. The achieved domain linewidth satisfies $d' = \sqrt{a^2\cos^2\theta + b^2\sin^2\theta}$. **b**, The calculated and measured domain widths at different θ.

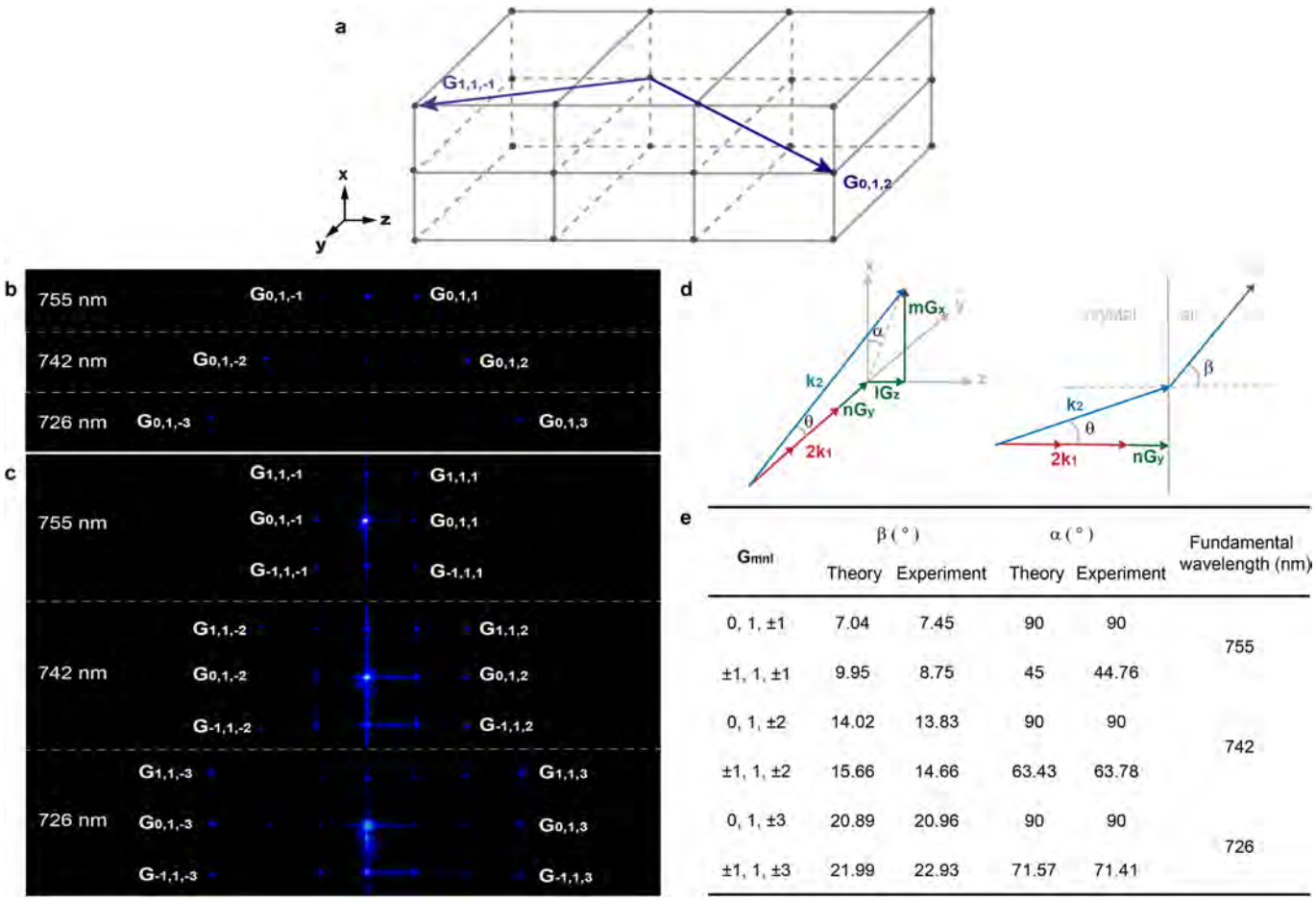

e

G_{mnl}	β (°)		α (°)		Fundamental wavelength (nm)
	Theory	Experiment	Theory	Experiment	
0, 1, ±1	7.04	7.45	90	90	755
±1, 1, ±1	9.95	8.75	45	44.76	
0, 1, ±2	14.02	13.83	90	90	742
±1, 1, ±2	15.66	14.66	63.43	63.78	
0, 1, ±3	20.89	20.96	90	90	726
±1, 1, ±3	21.99	22.93	71.57	71.41	

Extended Data Fig. 5 | SH generations in 2D and 3D periodic domain structures. a, The typical QPM configuration[45]. **b**, **c**, The QPM SH patterns in 2D and 3D $LiNbO_3$ domain structures, respectively. The intensities of the SH spots depend on whether the QPM condition is fully satisfied. At input fundamental wavelengths of 755 nm, 742 nm, and 726 nm, the non-collinear QPM SH generations from 2D domain array are realized by involving $G_{0,1,-1}/G_{0,1,1}$, $G_{0,1,-2}/\vec{G}_{0,1,2}$, and $G_{0,1,-3}/G_{0,1,3}$, respectively. The corresponding SH pattern presents two symmetric bright spots (**b**). In comparison to 2D case, the number of the SH spots from 3D domain structure clearly increases because the QPM condition is simultaneously satisfied by more reciprocal vectors (**c**). Notably, the central SH spot is bright because it is produced through a collinear SH generation process that has a much longer interaction length than those under non-collinear SH generation configurations. **d**, **e**, The measured and calculated emitting angles of the output SH beams.

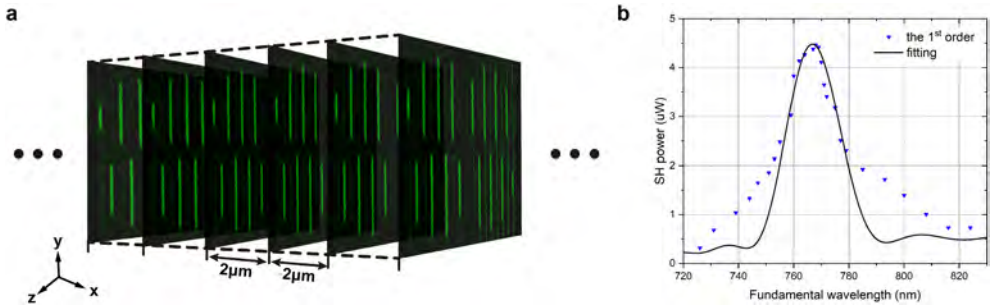

Extended Data Fig. 6 | SH HG-mode generation in a 3D nonlinear grating. **a**, A 3D $\chi^{(2)}$-grating structure for SH HG_{11} beam generation under 3D QPM condition[66]. **b**, The measured dependence of the SH power at the 1^{st} order on the fundamental wavelength. The 3D QPM condition is satisfied at 768 nm. The deviation in **b** can be attributed to the broad bandwidth of the input femtosecond laser and the limited period number of the domain structure.

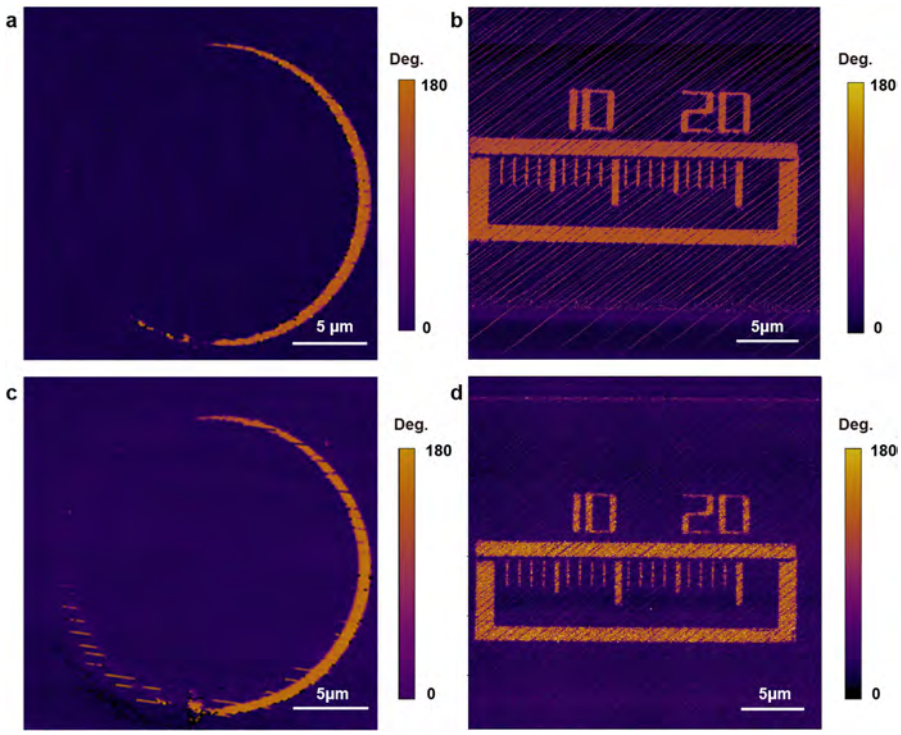

Extended Data Fig. 7 | Stability test of $LiNbO_3$ domain structures. a, The PFM image of a $LiNbO_3$ domain structure prepared by laser writing in Oct. 2019. After being kept at room temperature for over two years, one can clearly observe the domain structure (**c**). We also put the ruler-shaped nanodomain structure (**b**) in a tube furnace for an annealing treatment. The sample temperature is increased to 300 °C at a heating rate of about 10 °C/min. After 2-h heat treatment at 300 °C, the sample is naturally cooled down to room temperature. The domain structure successfully survives after such annealing process (**d**). The domain structures have no significant changes after a two-year storage or an annealing treatment.

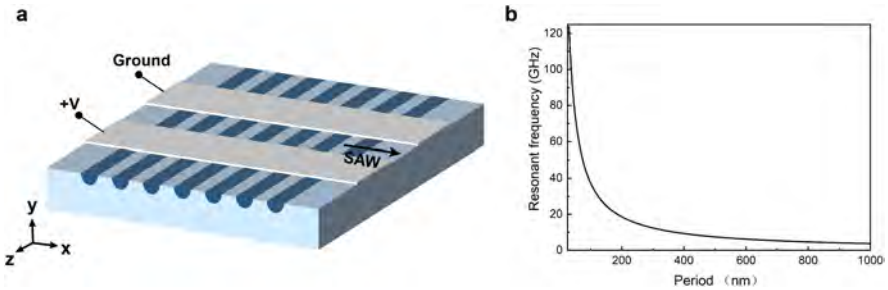

Extended Data Fig. 8 | Surface acoustic waves (SAW) generation in $LiNbO_3$ nanodomain arrays. a, The diagram of SAW device based on $LiNbO_3$ nanodomain array. In such $LiNbO_3$ domain structure (also called acoustic superlattice), the sign of the piezoelectric coefficients is periodically switched, which can produce SAW by using uniform electrodes. The SAW resonant frequency is given by[67] $f=\frac{v}{\lambda}$, where v is the SAW velocity, and λ is the acoustic wavelength that is equal to the period of the $LiNbO_3$ domain structure. **b**, The calculated dependence of SAW resonant frequency on the domain period. The SAW velocity is 3718 m/s[68]. For the nanodomain structures with periods of 100 nm and 50 nm, the SAW frequencies reach 37.2 GHz and 74.4 GHz, respectively.

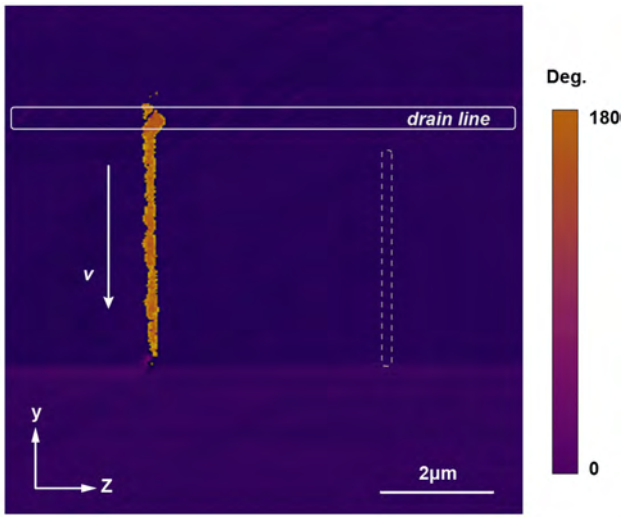

Extended Data Fig. 9 | Comparison of laser writing with/without the use of a drain line. The solid white line indicates the drain line. When laser writing starts from the drain line, one can produce a $LiNbO_3$ domain line (left). In contrast, under the same laser writing parameters, one cannot write $LiNbO_3$ domains without the use of drain line. The laser writing track is marked by the dashed white line (right). In experiment, we use conductive atomic force microscopy to measure the electric conductivity of drain line, which is several orders of magnitude higher than the value of $LiNbO_3$ crystal.

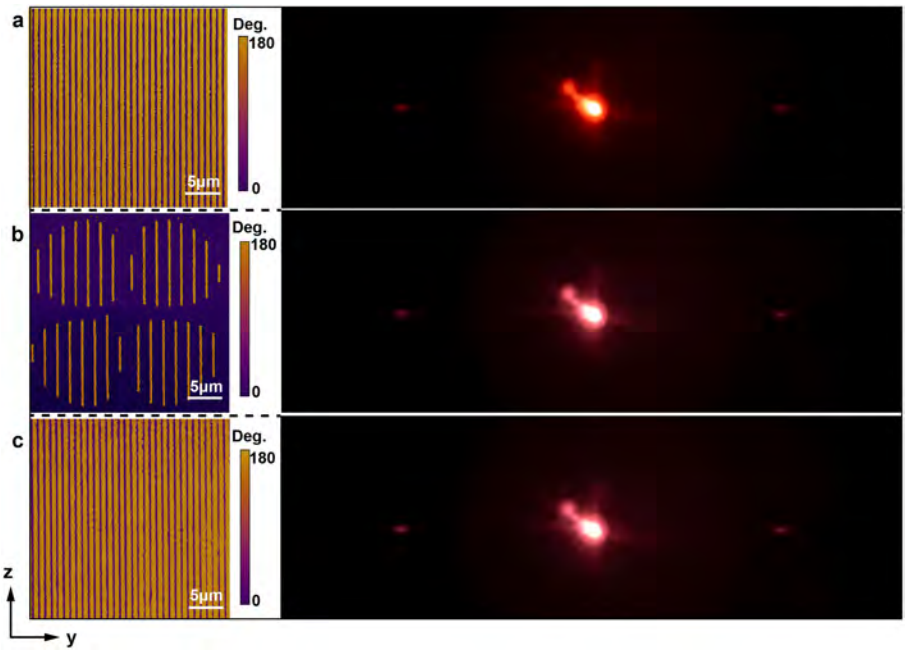

Extended Data Fig. 10 | The linear diffraction patterns from the gratings in Fig. 4a–c at an input wavelength of 690 nm. The non-zero diffraction order can be barely observed, which indicates no significant change in the refractive index.